

# Understanding the atmospheric response to seismic sources: the 2020 $m_b$ 4.9 Kiruna minequake, Sweden

Antoine Turquet [<https://orcid.org/0000-0003-1920-935X>]<sup>1</sup>, Quentin Brissaud [<https://orcid.org/0000-0001-8189-4699>]<sup>\*1</sup>, Celso Alvizuri [<https://orcid.org/0000-0002-3104-0756>]<sup>1</sup>, Sven Peter Näsholm [<https://orcid.org/0000-0001-9107-4002>]<sup>1,2</sup>, Alexis Le Pichon [<https://orcid.org/0000-0001-6531-069X>]<sup>3</sup>, and Johan Kero [<https://orcid.org/0000-0002-2177-6751>]<sup>4</sup>

<sup>1</sup>NORSAR, Gunnar Randers vei 15, Kjeller, Norway

<sup>2</sup>Department of Informatics, University of Oslo, P.O. Box 1080, NO-0316 Oslo, Norway

<sup>3</sup>CEA, DAM, DIF, F-91297 Arpajon, France

<sup>4</sup>Swedish Institute of Space Physics (IRF), Kiruna, Sweden

**Abstract.** A minequake of magnitude  $m_b$  4.9 occurred on 18 May 2020 early in the morning at the LKAB underground iron ore mine in Kiruna, Sweden. This is the largest mining-induced earthquake in Scandinavia. It generated acoustic signals observed at three infrasound arrays at 9.3 (KRIS, Sweden), 155 (IS37, Norway), and 286 km (ARCI, Norway) distance. Using regional seismic data, we performed 5 a moment-tensor inversion highlighting that this event was dominated by a shallow-depth collapse in agreement with in-mine seismic station data. This was further confirmed by full waveform modelling within a coupled Earth-atmosphere model at local and regional distances using full moment tensor sources. Discrepancies between epicentral location from regional seismic inversion and simulated acoustic data indicate that local pressure records can help further constraining a seismic event 10 location. Numerical simulations demonstrate a potential of using local and regional infrasound data to constrain focal mechanism and depth.

**Plain Language Summary.** The largest mining-induced earthquake in Scandinavia ( $m_b$  4.9) occurred on 18 May 2020 early in the morning at the LKAB underground iron ore mine in Kiruna, Sweden. The seismic waves coupled to the atmosphere and propagated large distances as sound 15 waves which were observed at three infrasound arrays at 9.3 (KRIS, Sweden), 155 (IS37, Norway), and 286 km (ARCI, Norway) distance. Our seismic and acoustic modeling results highlight a strong collapse event within the northern section of the mine. The successful modelling of signals across

the Earth-atmosphere suggests that sound waves can help constraining a seismic source at local and regional scales.

20

## Key Points

- Seismic and acoustic records indicate a strong collapse at shallow depth for the 2020 Kiruna minequake
- Local pressure records are in good agreement with in-mine seismic source inversions
- 25 – Focal mechanisms and depths can be retrieved from local and regional infrasound station records

## 1 Introduction

Underground seismic sources, e.g., earthquakes and man-made explosions, excite seismic waves that couple to the atmosphere and propagate as infrasound – low-frequency acoustic waves at 30 below 20 Hz – over great distance (*Donn and Posmentier, 1964; Dannemann Dugick et al., 2023*). Recent studies highlight correlations between earthquake magnitude, ground motion, and infrasound amplitude (*Hernandez et al., 2018; Vallage et al., 2021; Shani-Kadmiel et al., 2018; Mutschlecner and Whitaker, 2005*). However, few studies have investigated the relationships between focal depth and focal mechanism with the acoustic wavefield (*Shani-Kadmiel et al., 2021; Brissaud et al., 2021; Inchin et al., 2021; Yang et al., 2021*). *Shani-Kadmiel et al. (2021)*, as well as *Inchin et al. (2021)*, successfully recovered the main rupture mechanism properties of large-magnitude earthquakes at low frequency. However, these inversions benefited from large earthquake magnitude and favorable downwind station locations. There is a lack of datasets and studies that incorporate local and regional earthquake (or minequake) infrasound. Therefore, it remains challenging to link earthquake rupture 40 mechanism, subsurface velocity structure, topography, and atmospheric path effects to infrasound observations at local and regional distances.

Discriminating between source and path effects at large distance is difficult as path effects (e.g., atmospheric absorption, scattering, dispersion, and refraction) can significantly influence acoustic

---

\*Corresponding author: Quentin Brissaud (quentin@norsar.no)

waveforms. Since infrasound observations are typically reported at regional or global ranges, where  
45 path effects dominate ( $> 100$  km distance), the interpretation of infrasound to retrieve source physics  
is challenging (*Shani-Kadmiel et al.*, 2021). Even at closer ranges ( $< 100$  km), source directivity can  
significantly impact the epicentral infrasound along the surface to prevent observations in shadow  
zones (*Arrowsmith et al.*, 2012a). Theoretical and experimental studies of surface and buried explosions  
have provided seismo-acoustic coupling insights. In particular, the ratio between seismic and acoustic  
50 amplitudes depends greatly on focal depth (*Lai et al.*, 2021). Only sources at depths shallower than a  
wavelength excite evanescent seismic body waves that couple to the atmosphere as strong spherically  
propagating infrasound (*Godin*, 2011). Recently, remote seismically-induced infrasound observations  
from explosive sources have provided unique insights into seismic parameters such as ground shaking  
source depth (*Averbach et al.*, 2020; *Lai et al.*, 2021) and yield (*Kim and Pasquano*, 2022). Yet, due  
55 to the lack of high-quality local and regional data, there is a need for additional rupture mechanism  
studies based on epicentral infrasound.

In the current study, we leverage a unique local and regional infrasound data related to the 18  
May 2020 minequake in Kiruna, Sweden, (Fig. 1a) to address our lack of seismo-acoustic coupling  
mechanism understanding. This  $m_b$  4.9 minequake at 1:11:56.2 UTC (Solution from the University  
60 of Uppsala,  $67.83965^\circ\text{N}$ ,  $20.20759^\circ\text{E}$ , see Fig. 1b), was the highest-magnitude minequake in Sweden.  
The mine, operated by Luossavaara-Kiirunavaara AB (LKAB), is the world's largest underground  
iron ore mine (Fig. 1b). A recent in-mine and regional seismic analysis (*Dineva et al.*, 2022) concluded  
that this minequake involved a complex series of normal faulting events in the south of the mine  
(line AD in Fig. 1b) followed by collapse events in the north of the mine (line AC in Fig. 1b). In  
65 addition to seismic waves, strong epicentral ground-motion excited infrasound was recorded at KRIS,  
IS37, and ARCI, at respectively, 9.3, 155, and 286 km distance (Fig. 1c,d,e). Such observations of  
acoustic signals at both local and regional distances are unprecedented.

## 2 Data

### 2.1 Infrasound observations

70 We analyzed infrasound arrivals at the four-sensor KRIS array, near Kiruna, at the 10-sensor IS37  
array in Bardufoss, Norway, as well as the eight-sensor ARCI array in Karasjok, Norway (Fig. 1a).

Data from the infrasound arrays are processed using the Progressive Multi-Channel Correlations (PMCC) framework (*Cansi*, 1995).

The KRIS local infrasound shows clear seismic and epicentral acoustic arrivals at backazimuths 75 towards the northern section of the Kiruna mine with a dominant frequency at 2.5 Hz (Fig. 1d). Owing to the shallow focal depth, the conversion of evanescent seismic waves at the Earth-atmosphere interface can explain a generation and propagation of infrasound from the epicenter and along the surface (*Godin*, 2011). Arrivals with dominant frequency below 2.5 Hz are visible continuously a few seconds before and after the main epicentral acoustic arrival 30 s after the origin time. This variety 80 of low-amplitude signals might be due to several competing factors, including tropospheric refraction, spatially and temporally distributed rupture mechanisms, and interactions with subsurface velocity structures. The possible resonance of acoustic waves within the mine (*Downey et al.*, 2022), similar to wave resonance within magma conduits (*Lai et al.*, 2021), might facilitate seismicoacoustic coupling at a different location than the main epicenter.

85 At regional distances, IS37 and ARCI feature high-frequency arrivals with no significant energy below 1 Hz (Figs. 1c,e). We observe a slight increase in apparent velocity with time (0.33 to 0.35 km/s) indicating the arrival of higher-altitude refractions or reflections from the lower stratosphere. The combination of high-frequency arrivals and stratospheric refraction or reflection suggests a shadow-zone ducting contribution due to small-scale gravity-wave related structures (*Chunchuzov* 90 and *Kulichkov*, 2019; *Vorobeva et al.*, 2023). The slightly lower amplitudes at ARCI compared to IS37 can be explained both by greater source-receiver range and weaker ducting due to lower effective soundspeed ratio at ARCI because of smaller stratospheric along-track winds (Fig. 1a).

### 3 Moment tensor inversion using seismic data

We estimated the source mechanism by first obtaining seismic waveforms from broadband 3-component 95 stations within a 1500 km radius, including Swedish National Seismic Network stations (SNSN, *Lund et al.*, 2021). The data was corrected for instrument response and rotated into source-receiver frames. Removing stations with low signal-to-noise ratios or low overall quality reduced the number of stations to 93. Our moment tensor analysis used Rayleigh and Love waveforms bandpass filtered between 0.05 – 0.2 Hz.

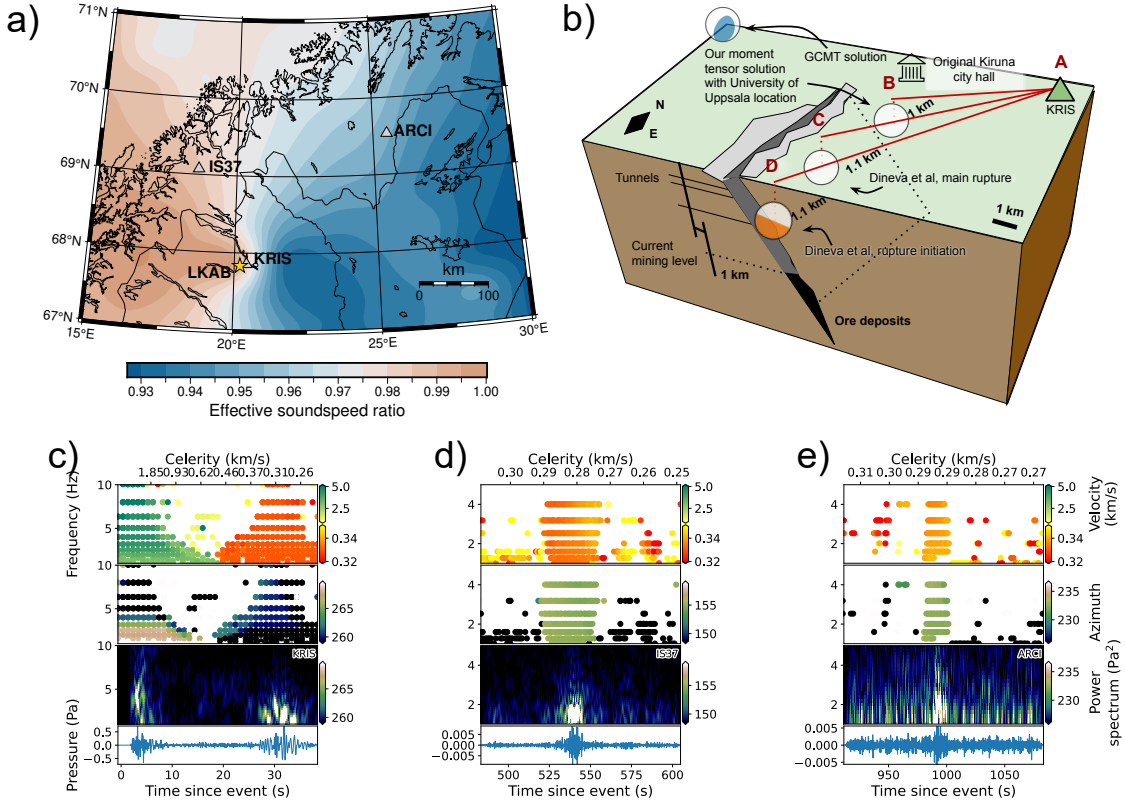


**Figure 1.** (a) Location of the 2020 Kiruna minequake epicenter (yellow star) and the infrasound arrays of this study (triangles). The background colors indicate the ratio between stratospheric (35–60 km altitude) and ground-level effective soundspeeds. (b) 3D mine sketch and the KRIS array location (label A), our moment tensor solution (label B), and locations of main source types from (*Dineva et al., 2022*) (labels C and D). (c,d,e) PMCC processing output for KRIS, IS37, and ARCI showing, from top to bottom, the apparent velocity, backazimuth, energy, and beamformed pressure vs time and frequency.

The moment tensors and the associated uncertainties were computed using a grid-search in moment-tensor space (*Alvizuri et al., 2018*) with the following steps: 1) computing synthetic seismograms for each mechanism, 2) calculating the misfit between observed and synthetic seismograms, and 3) identifying the mechanism with the smallest misfit. We did not invert for source location nor origin time and used the solution described in Sec. 2.1. The synthetic seismograms were computed using a CRUST1.0 1D (*Laske et al., 2013*) velocity model (Supp. Sec. 5). The moment-tensor uncertainties were computed from ensemble solutions appraised in the grid search.

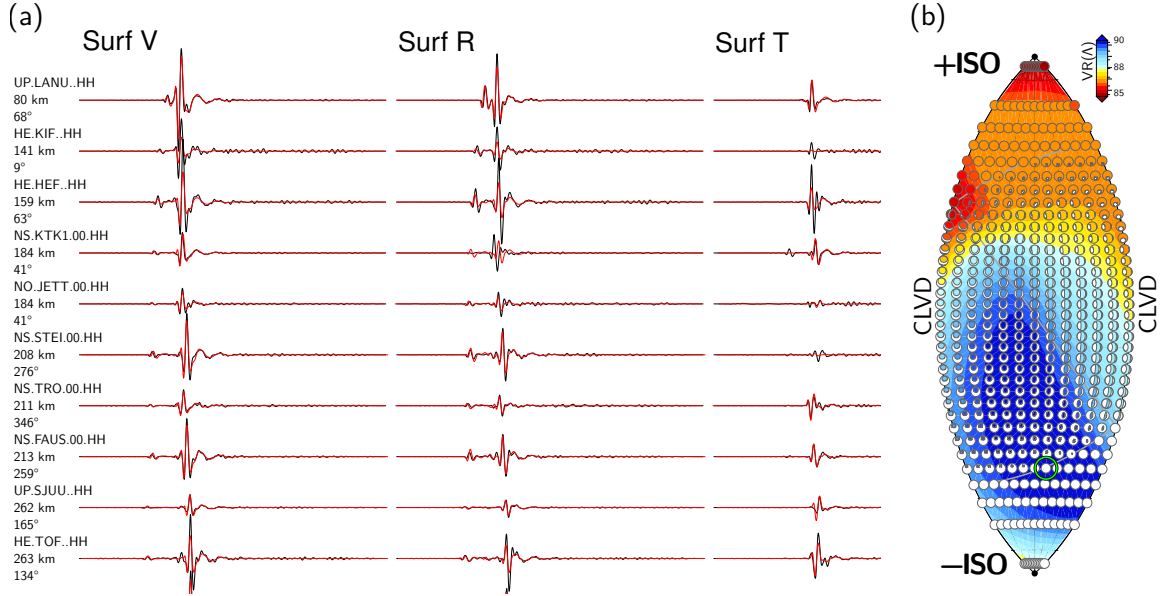


**Figure 2.** Moment tensor estimation results. (a) Comparison between recorded (black) and synthetic (red) seismic waveforms for the ten closest stations out of 93 stations (see Supp Section 6). (b) Full grid search summary on a lune diagram, showing the best-fitting solution at each grid point on the lune and colored by waveform fit, with best-fitting solutions in blue and worst-fitting solutions in red.

The results show a best fitting mechanism with primarily negative isotropic source parameters (Fig. 2 and Supp. Sec. 6). The corresponding seismograms show good agreement between observations and synthetics. Figure 2b summarizes the grid search results on a source-type diagram, or lune.

110 The lune organizes moment tensors by source-types, with positive isotropic solutions on top of the lune (usually related to explosion mechanisms), negative isotropic at the bottom (e.g., implosion or collapse), and double-couple at the center (e.g., tectonic earthquakes). The best-fitting solutions are concentrated in the negative isotropic source-type and the worst-fitting solutions are towards the positive isotropic.

#### 115 4 Local seismo-acoustic propagation modeling

Infrasound backazimuth data provide epicentral ground shaking constraints corresponding to regions of high seismic-to-acoustic energy transfer (*Hernandez et al.*, 2018). Assuming a great circle propagation path, we can backproject coherent local infrasound along the estimated backazimuth to estimate

the Transmission Loss (TL) around the source (see Supp. Sec. 2). We considered an origin time at  
120 01:11:56 UTC with error  $\pm 3$  s. Furthermore the following distributions of sound velocity  $c_s = 330 \pm 8$  m/s, and backazimuth error  $e_{baz} = \pm 5$  degrees were used for inversion. The maximum SPL location fits the moment tensor solutions in the northern section of the mine (Fig. 3a) but large TLs also spread along the propagation, most likely highlighting a temporal distribution of acoustic source sub-events.

125 To investigate the sensitivity of infrasound and seismic phases to focal depth and mechanism, we ran full-waveform simulations of the coupled Earth-atmosphere system using SPECFEM2d-DG (*Brissaud et al.*, 2017; *Martire et al.*, 2022). This modeling tool simulates both seismic and acoustic wave propagation from a moment-tensor point source. We applied Gaussian source-time functions with unit integral and half duration 2 s. Because we performed 2D instead of 3D simulations, we first  
130 projected the full moment tensor along the azimuth between the epicenter and our receiver (*Brissaud et al.*, 2021) and corrected for spherical geometrical spreading considering a linear propagating path (Supp. Sec. 3). The simulated acoustic wavefield (Fig. 3b) for a shallow collapse event at 0.5 km depth (Sec. 3) indicates the presence of four major seismic-to-acoustic phase arrivals: 1) low-amplitude planar wavefronts generated by scattered P waves (PI); 2) planar wavefronts due to Rayleigh waves (RWI); 3)  
135 spherical wavefronts excited by evanescent body waves (SI); 4) upward propagating wavefronts excited by direct body waves followed by upward propagating signal produced by body-wave reflections on the shallowest velocity layer (EI).

Numerical solutions using the original Uppsala solution show a 1 s time shift between true and simulated EI arrivals, i.e., an event location error (black and purple lines in Fig. 3c). By translating  
140 the epicenter about 340 m, i.e., 1 s at 340 m/s, towards the Northern section of the mine ( $67.8391^\circ\text{N}$ ,  $20.1997^\circ\text{E}$ ) leads to a much better fit between the true and synthetic solutions (red line in Fig. 3c). Variations in focal depths show that solutions shallower than 1 km are unable to reproduce accurately  
145 the arrivals at KRIS (black line in Fig. 3c). This is clearly visible when computing the Mean Absolute Error (MAE) between synthetic and recorded waveforms where error is minimized for a solution below 1 km depth (Fig. 3d). Although simulated seismic amplitudes do not vary significantly with focal depth, acoustic amplitudes drastically decrease for deep solutions, especially at high frequencies (Fig. 3e). Other regional moment tensor solutions, such as the Global Centroid Moment Tensor (GCMT, orange line, Fig. 3c), do not capture the observed seismic-to-acoustic ratio and phase owing to the lack of isotropic component. Topography is important to accurately model the full acoustic  
150 wavefield at high frequency (*Fee et al.*, 2021; *Brissaud et al.*, 2021). However, our simulations with

and without topography show that the influence of topography is insignificant on local infrasound in the frequency range of interest (Supp. Sec. 4).

Our numerical results are in agreement with in-mine seismic inversions performed by *Dineva et al.* (2022) which highlighted that the largest magnitude events occurred north of the mine as collapse events at about 1 km depth (labels C and B in Fig. 3b). Additionally, *Dineva et al.* (2022) showed that the minequake was initiated in the southern section of the mine with normal-fault events at  $\sim 1$  km depth. To assess whether the observed arrival times and phases correspond to events in the northern or southern section of the mine, we simulated a collapse event  $\sim 3$  km south of our initial solution at 0.5 km depth (Supp. Sec. 4). The results show a significant delay in acoustic arrivals, compared to our initial epicentral location, and do not fit the observed arrivals. This suggests that the observed arrivals originate from the northern section of the mine. The good phase fit suggests that local infrasound recordings can help discriminating between focal mechanism solutions.

Yet, the modelling is unable to capture the higher frequency content above 0.5 Hz (Top signal in Fig. 3c). This discrepancy owes to several factors, including competing effects between temporal and spatial slip distribution at shallow depths (*Vallage et al.*, 2021), mine geometry (*Downey et al.*, 2022), and unresolved subsurface velocity structures (*Martire et al.*, 2018). In the case of the Le Teil earthquake, the significant near-surface vertical slip was the likely the dominant infrasound source (*Vallage et al.*, 2021). For the Kiruna minequake, *Dineva et al.* (2022) mentioned the possibility of surface landslides. Such events would generate high-frequency signals at KRIS. Tunnel resonance exciting acoustic waves might also contribute to the higher frequencies observed at KRIS (*Downey et al.*, 2022). The influence of shallow seismic stratification on seismic-to-acoustic energy transfer is poorly understood. To qualitatively assess its influence on simulated KRIS waveforms, we considered a model with a 200 m horizontal layer with 0.5 km/s shear velocity (Supp. Sec. 4). These simulations suggest that shallow velocity layers are key to account for when their thickness match the frequency range of interest which is not the case here below 0.7 Hz.

## 5 Regional infrasound propagation modeling

Wave propagation simulations using atmospheric models like ERA5 typically do not reproduce the observed shadow-zone arrivals from blasts at regional infrasound stations (*Blixt et al.*, 2019; *Vera Rodriguez et al.*, 2020; *Amezcu et al.*, 2020). The presence of small-scale gravity-wave perturbations generally explains the refraction of infrasound energy back to the surface (*Chunchuzov and Kulichkov*,

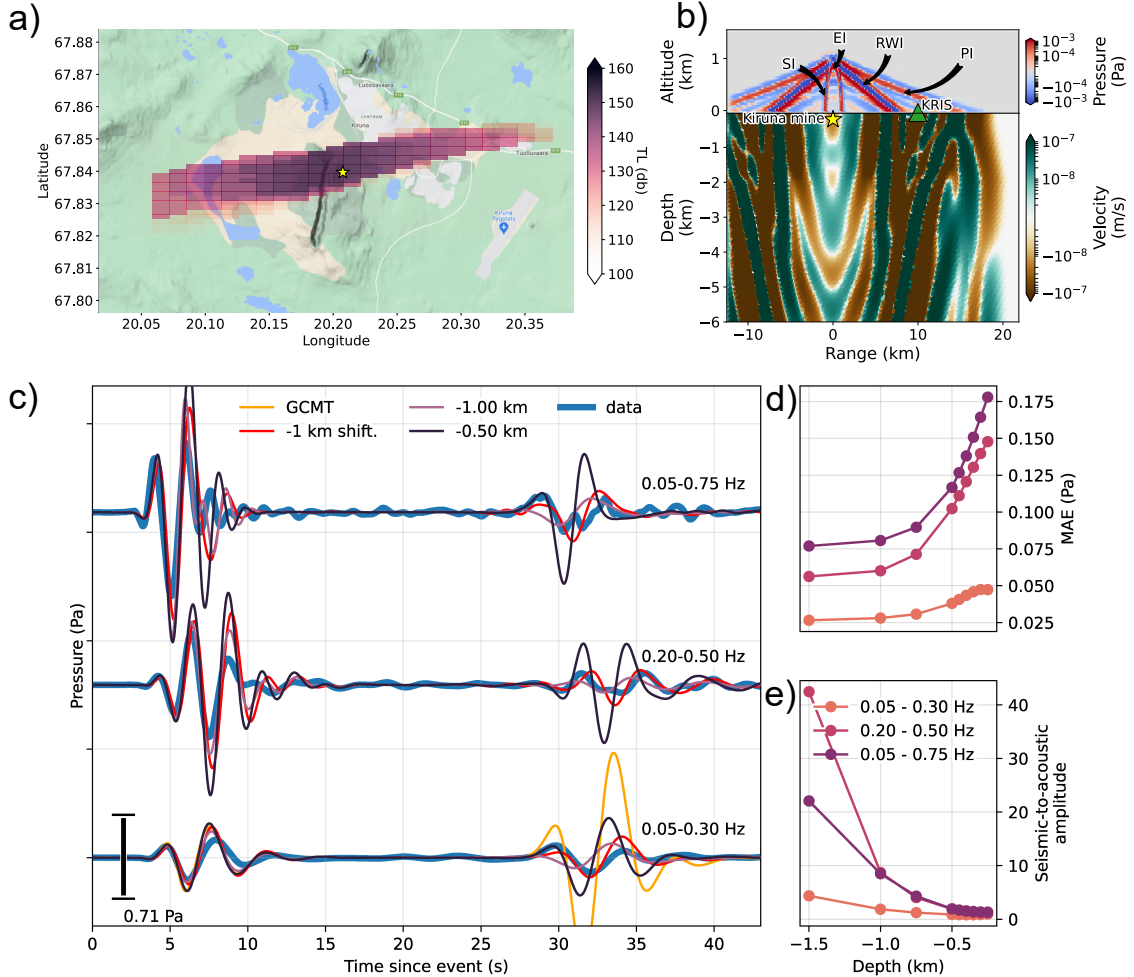


**Figure 3.** Local full-waveform modeling. (a) back-projected Transmission-Loss (TL in db, with a normalization factor of 1 Pa) using KRIS data. The star corresponds to the epicenter. (b) Seismo-acoustic wavefield snapshot generated from a shallow collapse event with Epicentral Infrasound (EI), Spherical Infrasound (SI), Rayleigh Wave Infrasound (RWI), and P-wave Infrasound (PI). (c) Recorded (thick blue), and simulated waveforms for the GCMT moment-tensor solution (orange), and our moment tensor solution at various depths (light pink, purple, and black). (d) Mean Absolute Error (MAR) between simulated and recorded waveforms for three frequency bands. (e) Seismic arrival-to-acoustic arrival amplitude ratio in the simulated pressure data.

2019; Vorobeva *et al.*, 2023). Moreover, it is challenging to build an accurate description of the source without local recordings.

We model regional signals using local recordings at KRIS, corrected for geometric spreading, as source-time function (*Averbach et al.*, 2022). This assumption also means that topography and source directivity effects (focal depth and mechanism) are insignificant. These assumptions are supported by two observations: 1) The high-frequency signals observed at KRIS, IS37 and ARCI were most likely excited by events close to the surface, which emit more energy along the surface compared to the main seismic event; 2) The seismic moment tensor solution explaining the observed low-frequency energy at KRIS is dominated by a collapse component, which is mostly isotropic and not azimuth dependent.

Similar to *Arrowsmith et al.* (2012b), we then model regional infrasound by considering that the source can be represented by a surface point-source at the epicenter. This enables us to simulate propagation into the far-field up to 10 Hz using the broadband normal-mode numerical simulator ModBB (*Waxler et al.*, 2021). This scenario would be overly computationally expensive using Galerkin full-waveform simulators such as SPECFEM-DG. The simulations were ran at a frequency step  $\Delta f = 2 \times 10^{-3}$  Hz. The atmospheric profiles used for these simulations are range-independent and were built from ERA5 reanalysis models extracted at the epicenter together with six gravity-wave realizations using Gardner model (see Supp. Sec. 1 and *Gardner et al.*, 1993).

The 2D transmission-loss maps at 1.5 Hz between source and receiver for the best atmospheric model, i.e., the model leading to the largest regional infrasound amplitude, show that arrivals at IS37 (Fig. 4ab) and ARCI (Fig. 4fg) correspond to a combination of waves refracted at various altitudes. Back-scattering to ground level is facilitated by small-scale gravity wave inhomogeneities. This back-scattering, from around midway between source and a station, facilitates the ducting of the main arrivals at IS37 and occurs at lower (25 – 30 km) altitude than for ARCI (40 – 45 km), because IS37 closer than ARCI. The best atmospheric models correspond to a good match with the recorded time signal envelopes at both IS37 and ARCI (Figs 4c,d,h,i). *Hernandez et al.* (2018) suggested that regional infrasound data can provide constraints on Surface Pressure Level (SPL) around the epicenter for accurate TL estimates. Our TL predictions at 1.5 Hz yield an epicentral SPL, at 0.2 km from the source, of  $\sim 0.3$  Pa using either ARCI or IS37 peak pressure readings. This clearly underestimates the SPL estimated at  $\sim 50$  Pa using KRIS peak pressure.

Other gravity wave realizations lead to significantly lower amplitudes (bottom panels of Figs 4d,i). Simulated energy distributions for the best atmospheric models seem to predict an energy peak 1.5 Hz at IS37 and 1.8 Hz at ARCI, which is consistent with the observations (Fig 4e), but overpredict the amplitude of frequency peaks at higher frequencies. This discrepancy highlights that

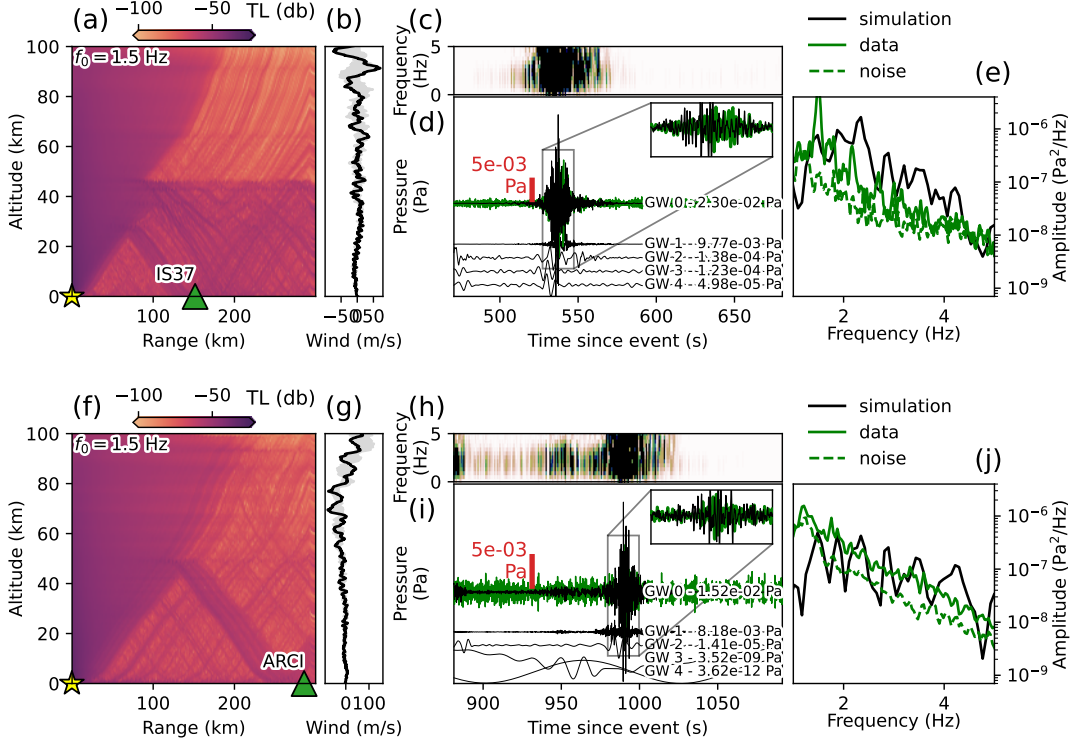


**Figure 4.** Regional infrasound data modelling at (a,b,c,d,e) IS37 and (f,g,h,i,j) ARCI. (a,f) Transmission loss vs range and altitude for the best atmospheric model along with (b,g) along-track winds (black) and wind amplitudes for other gravity-wave realizations (shaded grey). (c,h) spectrograms computed from the best-fitting numerical solutions. (d,i) recorded (green) and simulated (black) signals for different gravity-wave realizations. The amplitudes are scaled independently for each realization. (e,j) Power Spectral Density for recorded (orange), recorded noise (blue), and simulated signals (black).

215 our best atmospheric model is not a true description of the atmosphere. Infrasound multipathing is visible at ARCI with an early arrival about 30 s before the main arrival. This might be a true atmospheric path effect, given that coherent energy is visible about 510 and 520 s (Fig 1c).

Our best atmospheric models, capturing the main features of the regional observations, provide an opportunity to accurately model infrasound and to assess whether focal mechanisms and depths 220 can be discriminated at large distances. We model these signals using the synthetic waveforms above the epicenter as source-time functions. These source-time functions are averaged between three

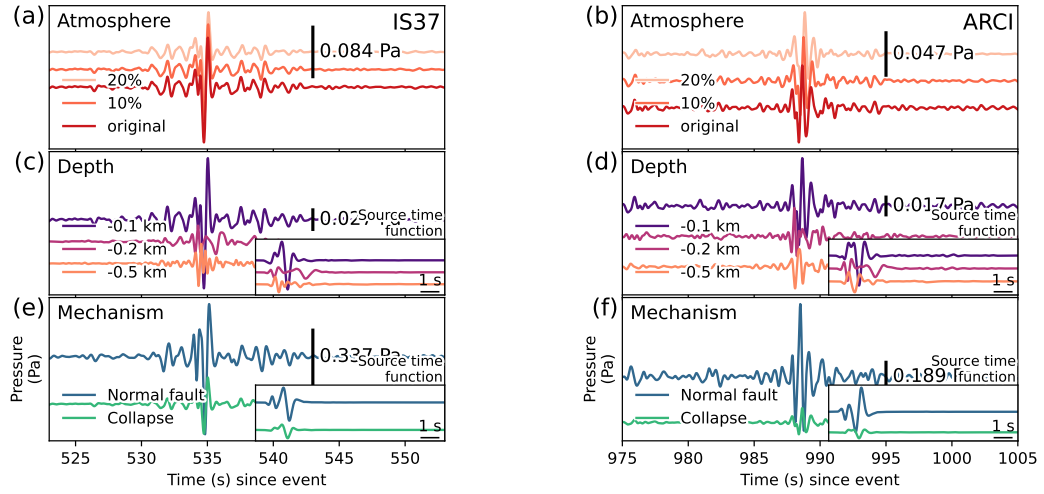


**Figure 5.** Atmospheric and source parameters effects on regional infrasound. Simulated waveforms for (a,b) varying gravity-wave amplitudes. The percentages correspond to a percentage of amplitude reduction compared to the original gravity wave realization, (c,d) varying focal depth, (e,f) varying source mechanism at IS37 (a,c,e), and ARCI (b,d,f). The source-time functions are shown in the inset panels of (c,d,e,f).

different launch angles corresponding to waves refracting back to both IS37 (30 – 35 degrees from vertical) and ARCI (40 – 45 degrees from vertical).

While the gravity-wave realizations have significant impact on regional infrasound phase and amplitude, small amplitude variations of a given gravity-wave realization has an insignificant effect on the signal characteristics (Fig. 5a,b). Focal depth and mechanism greatly influence the arrival time and overall energy distribution of the local infrasound. Similarly, simulated regional signals are dominated by the negative of the original signals (Fig. 5c,d,e,f) which generally corresponds to waves travelling through 2nd order caustics, i.e., the intersection between slow arrival reflection caustic branches with the shadow zone caustic branches (Waxler *et al.*, 2015). Comparing IS37 (Fig. 5a,c,e) and ARCI (Fig. 5b,d,f) we note that a larger-scale change in atmospheric properties together with different travel paths severely impact the energy distribution of the main infrasound arrivals.

## 6 Conclusions

The 2020 Kiruna minequake was the largest-ever recorded mining-induced seismic event in Sweden.

- 235 For the first time ever, the epicentral infrasound signature of a shallow seismic event was detected at both local and regional distances. Both regional seismic waveforms and local infrasound were accurately modeled below, respectively, 0.25 and 0.7 Hz. Both seismic and acoustic records show a clear signature of a shallow collapse event at about 1 km depth in the northern section of the Kiruna mine. This solution is in agreement with the in-mine seismic records (*Dineva et al., 2022*).
- 240 Discrepancies between simulated and observed signals above 0.5 Hz can be explained by various seismic-to-acoustic coupling effects exciting strong acoustic waves. This includes tunnel resonance, surface slip, and unconstrained shallow seismic velocities.

Regional simulations using realistic atmospheric models together with a realization of gravity wave perturbations match well the observed signal envelopes at IS37 and ARCI despite discrepancies in terms of energy distribution at high frequencies. This good fit benefited from the use of local records at KRIS which captures accurately the source effects. Our numerical sensitivity analysis highlighted a strong correlation between regional and local infrasound for varying focal depths and mechanisms. Such strong correlations allows us to map regional infrasound to specific source characteristics for cases when the infrasound path is known and for large-enough signal-to-noise ratios.

- 250 However, the quality of the source mechanism retrieval depends on the atmospheric model accuracy used in the the infrasound propagation modelling (*Averbach et al., 2022*). Therefore, future research could explore a wider range of possible atmospheric profiles using all ensemble members as well as a larger number of gravity-wave realizations to assess the uniqueness of the synthetic solutions. Additionally, finite-size sources should be preferred instead of point sources, using Earth-atmosphere 255 coupled full-waveform simulations. It will be key in future studies to understand how uncertainties in both seismic sub-event and seismic velocitiy distribution impact the broadband seismic-to-acoustic energy transfer. Nevertheless, the combination of full-waveform seismo-acoustic simulations in the near field and normal mode simulations in the far field provides a practical framework to analyze seismically induced infrasound.

- 260 This study highlighted the potential of using local and regional infrasound recordings to assess seismic events in regions of poor seismic coverage (*Shani-Kadmiel et al., 2021*). Importantly, the good phase and amplitude fits between simulated and observed signals suggest that explosive sources can be discriminated from collapse events in pressure recordings, since the resulting explosive waveforms

show an opposite sign compared to collapse waveforms. This can be particularly valuable when  
265 discriminating between nuclear explosions, earthquakes, and other seismic sources in remote regions. The detection of seismically-induced infrasound and a better understanding of seismo-acoustic coupling mechanisms might also be key when exploring other planets' interiors, such as Venus (*Brissaud et al.*, 2021; *Garcia et al.*, 2022).

### Acknowledgements

270 Quentin Brissaud and Antoine Turquet contributed equally to this work. The authors thank Tormod Kvaerna for valuable insight and advice during this work. This work received support from the *Airborne Inversion of Rayleigh wave* (AIR) project, funded by the Research Council of Norway basic research program FRIPRO/FRINATEK, Contract 335903, and the *Middle Atmosphere Dynamics: Exploiting Infrasound Using a Multidisciplinary Approach at High Latitudes* (MADEIRA) project, 275 funded by the Research Council of Norway basic research program FRIPRO/FRINATEK, Contract 274377, as well as NORSAR institute funding.

### Author contributions

Conceptualization: ALP, AT, SPN, QB, CA

Supervision: AT, QB, SPN, ALP

280 Methodology and Formal analysis: QB, CA, ALP, SPN

Investigation: AT, QB, SPN, ALP

Visualization: QB, SPN, CA, AT

Writing – original draft: QB, AT, SPN, CA

Writing – review and editing: QB, AT, SPN, ALP, JK, CA

### 285 Competing interests

The authors declare that they have no competing interests.

## Data Availability Statement

Recorded and synthetic waveform data will be made available upon acceptance of the manuscript. The SPECFEM-DG code is available at <https://github.com/samosa-project/specfem2d-dg>. The ModBB  
290 normal mode code is available at <https://github.com/chetzer-ncpa/ncpaprop-release>. The code to produce gravity-wave realizations is available at [https://github.com/QuentinBrissaud/gardner\\_perturbations](https://github.com/QuentinBrissaud/gardner_perturbations). The IS37 infrasound station is part of the International Monitoring System of the Preparatory Commission for the Comprehensive Nuclear-Test-Ban Treaty Organization. Data access can be granted to third parties and researchers through the virtual Data Exploitation Centre:  
295 <https://www.ctbto.org/specials/vdec/>. Seismic data from the Swedish National Seismic Network is available upon request through <https://doi.org/10.18159/SNSN>. Infrasound data from the ARCI and KRIS stations will be made available upon acceptation of the manuscript. Moment tensor solutions are available at [http://www.isc.ac.uk/cgi-bin/web-db-run?event\\_id=618291845&zout\\_format=ISF2&request=COMPREHENSIVE](http://www.isc.ac.uk/cgi-bin/web-db-run?event_id=618291845&zout_format=ISF2&request=COMPREHENSIVE).

300 **References**

- Alvizuri, C., V. Silwal, L. Krischer, and C. Tape (2018), Estimation of full moment tensors, including uncertainties, for nuclear explosions, volcanic events, and earthquakes, *Journal of Geophysical Research: Solid Earth*, 123(6), 5099–5119.
- Amezcu, J., S. P. Näsholm, E. M. Blixt, and A. J. Charlton-Perez (2020), Assimilation of atmospheric infrasound data to constrain tropospheric and stratospheric winds, *Quarterly Journal of the Royal Meteorological Society*, 146(731), 2634–2653.
- Arrowsmith, S. J., R. Burlacu, K. Pankow, B. Stump, R. Stead, R. Whitaker, and C. Hayward (2012a), A seismoacoustic study of the 2011 January 3 Circleville earthquake, *Geophysical Journal International*, 189(2), 1148–1158, <https://doi.org/10.1111/j.1365-246X.2012.05420.x>.
- Arrowsmith, S. J., R. Burlacu, K. Pankow, B. Stump, R. Stead, R. Whitaker, and C. Hayward (2012b), A seismoacoustic study of the 2011 January 3 Circleville earthquake: Seismoacoustic study: Circleville earthquake, *Geophysical Journal International*, 189(2), 1148–1158, <https://doi.org/10.1111/j.1365-246X.2012.05420.x>.
- Averbuch, G., R. M. Waxler, P. S. Smets, and L. G. Evers (2020), Probabilistic inversion for submerged source depth and strength from infrasound observations, *The Journal of the Acoustical Society of America*, 147(2), 1066–1077, <https://doi.org/10.1121/10.0000695>.
- Averbuch, G., M. Ronac-Giannone, S. Arrowsmith, and J. Anderson (2022), Evidence for short temporal atmospheric variations observed by infrasonic signals: 1. the troposphere, *Earth and Space Science*, 9(3), e2021EA002,036, <https://doi.org/10.1029/2021EA002036>.
- Blixt, E. M., S. P. Näsholm, S. J. Gibbons, L. G. Evers, A. J. Charlton-Perez, Y. J. Orsolini, and T. Kværna (2019), Estimating tropospheric and stratospheric winds using infrasound from explosions, *The Journal of the Acoustical Society of America*, 146(2), 973–982, ISBN: 0001-4966 Publisher: Acoustical Society of America.
- Brissaud, Q., R. Martin, R. F. Garcia, and D. Komatitsch (2017), Hybrid Galerkin numerical modelling of elastodynamics and compressible Navier–Stokes couplings: applications to seismo-gravito acoustic waves, *Geophysical Journal International*, 210(2), 1047–1069, <https://doi.org/10.1093/gji/ggx185>.
- Brissaud, Q., S. Krishnamoorthy, J. M. Jackson, D. C. Bowman, A. Komjathy, J. A. Cutts, Z. Zhan, M. T. Pauken, J. S. Izraelevitz, and G. J. Walsh (2021), The first detection of an earthquake from a balloon using its acoustic signature, *Geophysical Research Letters*, 48(12), e2021GL093,013, <https://doi.org/10.1029/2021GL093013>.
- Cansi, Y. (1995), An automatic seismic event processing for detection and location: The PMCC method, *Geophysical Research Letters*, 22(9), 1021–1024.
- Chunchuzov, I., and S. Kulichkov (2019), Internal gravity wave perturbations and their impacts on infrasound propagation in the atmosphere, in *Infrasound monitoring for atmospheric studies*, pp. 551–590, Springer, [https://doi.org/10.1007/978-3-319-75140-5\\_16](https://doi.org/10.1007/978-3-319-75140-5_16).

- 335 Dannemann Dugick, F., C. Koch, E. Berg, S. Arrowsmith, and S. Albert (2023), A New Decade in Seismoacoustics (2010–2022), *Bulletin of the Seismological Society of America*, <https://doi.org/10.1785/0120220157>.
- Dineva, S., C. Dahnér, D. Malovichko, and L. Rudzinski (2022), Analysis of the magnitude 4.2 seismic event on 18 may 2020 in the Kiirunavaara mine, Sweden, in *Proceedings of the Tenth Conference on Rockburst and Seismicity in Mines, Society for Mining, Metallurgy and Exploration, Englewood*.
- 340 Donn, W. L., and E. S. Posmentier (1964), Ground-coupled air waves from the great alaskan earthquake, *Journal of Geophysical Research*, 69(24), 5357–5361.
- Downey, N., S. Albert, and R. Tibi (2022), The Redmond salt mine monitoring experiment: Observations of infrasound resonance, *Bulletin of the Seismological Society of America*.
- Fee, D., L. Toney, K. Kim, R. W. Sanderson, A. M. Iezzi, R. S. Matoza, S. De Angelis, A. D. Jolly, J. J. 345 Lyons, and M. M. Haney (2021), Local explosion detection and infrasound localization by reverse time migration using 3-D finite-difference wave propagation, *Frontiers in Earth Science*, 9, 620,813.
- Garcia, R. F., A. Klotz, A. Hertzog, R. Martin, S. Gérier, E. Kassarian, J. Bordereau, S. Venel, and D. Mimoun (2022), Infrasound from large earthquakes recorded on a network of balloons in the stratosphere, *Geophysical Research Letters*, 49(15), e2022GL098,844.
- 350 Gardner, C. S., C. A. Hostetler, and S. J. Franke (1993), Gravity wave models for the horizontal wave number spectra of atmospheric velocity and density fluctuations, *Journal of Geophysical Research: Atmospheres*, 98(D1), 1035–1049.
- Godin, O. A. (2011), Low-frequency sound transmission through a gas–solid interface, *The Journal of the Acoustical Society of America*, 129(2), EL45–EL51.
- 355 Hernandez, B., A. L. Pichon, J. Vergoz, P. Herry, L. Ceranna, C. Pilger, E. Marchetti, M. Ripepe, and R. Bossu (2018), Estimating the ground-motion distribution of the 2016 Mw 6.2 Amatrice, Italy, earthquake using remote infrasound observations, *Seismological Research Letters*, 89(6), 2227–2236, <https://doi.org/10.1785/0220180103>.
- Inchin, P., J. Snively, Y. Kaneko, M. Zettergren, and A. Komjathy (2021), Inferring the evolution of a large 360 earthquake from its acoustic impacts on the ionosphere, *AGU Advances*, 2(2), e2020AV000,260.
- Kim, K., and M. E. Pasanos (2022), Yield estimation of the august 2020 Beirut explosion by using physics-based propagation simulations of regional infrasound, *Geophysical Research Letters*, p. e2022GL101118.
- Lai, V. H., Z. Zhan, Q. Brissaud, O. Sandanbata, and M. S. Miller (2021), Inflation and asymmetric collapse at Kīlauea summit during the 2018 eruption from seismic and infrasound analyses, *Journal of Geophysical 365 Research: Solid Earth*, 126(10), e2021JB022,139, <https://doi.org/10.1029/2021JB022139>.
- Laske, G., G. Masters, Z. Ma, and M. Pasanos (2013), Update on CRUST1.0 – A 1-degree global model of Earth’s crust, in *Geophysical research abstracts*, vol. 15, p. 2658, EGU General Assembly Vienna, Austria.
- Lund, B., P. Schmidt, Z. Hossein Shomali, and M. Roth (2021), The Modern Swedish National Seismic Network: Two Decades of Intraplate Microseismic Observation, *Seismological Research Letters*, 92(3), 370 1747–1758, <https://doi.org/10.1785/0220200435>.

- Martire, L., Q. Brissaud, V. H. Lai, R. F. Garcia, R. Martin, S. Krishnamoorthy, A. Komjathy, A. Cadu, J. A. Cutts, J. M. Jackson, D. Mimoun, M. T. Pauken, and A. Sournac (2018), Numerical simulation of the atmospheric signature of artificial and natural seismic events, *Geophys. Res. Lett.*, 45(21), <https://doi.org/10.1029/2018GL080485>.
- 375 Martire, L., R. Martin, Q. Brissaud, and R. F. Garcia (2022), Specfem2d-dg, an open-source software modelling mechanical waves in coupled solid–fluid systems: the linearized navier–stokes approach, *Geophysical Journal International*, 228(1), 664–697.
- Mutschlechner, J. P., and R. W. Whitaker (2005), Infrasound from earthquakes, *J. Geophys. Res.*, 110(D1), D01,108, <https://doi.org/10.1029/2004JD005067>.
- 380 Shani-Kadmiel, S., G. Averbach, P. Smets, J. Assink, and L. Evers (2021), The 2010 Haiti earthquake revisited: An acoustic intensity map from remote atmospheric infrasound observations, *Earth and Planetary Science Letters*, 560, 116,795, <https://doi.org/10.1016/j.epsl.2021.116795>.
- Shani-Kadmiel, S., J. D. Assink, P. S. M. Smets, and L. G. Evers (2018), Seismoacoustic coupled signals from earthquakes in central Italy: epicentral and secondary sources of infrasound, *Geophysical Research Letters*, 45(1), 427–435, <https://doi.org/10.1002/2017GL076125>.
- 385 Vallage, A., L. Bollinger, J. Champenois, C. Duverger, A. G. Trilla, B. Hernandez, A. L. Pichon, C. Listowski, G. Mazet-Roux, M. Menager, B. Pinel-Puysségur, and J. Vergoz (2021), Multitechnology characterization of an unusual surface rupturing intraplate earthquake: the ML 5.4 2019 Le Teil event in France, *Geophysical Journal International*, 226(2), 803–813, <https://doi.org/10.1093/gji/ggab136>.
- 390 Vera Rodriguez, I., S. P. Näsholm, and A. Le Pichon (2020), Atmospheric wind and temperature profiles inversion using infrasound: An ensemble model context, *The Journal of the Acoustical Society of America*, 148(5), 2923–2934.
- Vorobeva, E., J. D. Assink, P. J. Espy, T. Renkwitz, I. P. Chunchuzov, and S. P. Näsholm (2023), Probing gravity waves in the middle atmosphere using infrasound from explosions, *Authorea Preprints*.
- 395 Waxler, R., L. G. Evers, J. Assink, and P. Blom (2015), The stratospheric arrival pair in infrasound propagation, *The Journal of the Acoustical Society of America*, 137(4), 1846–1856.
- Waxler, R., C. Hetzer, J. Assink, and D. Velea (2021), chetzer-ncpa/ncpaprop-release: NCPAprop v2.1.0, <https://doi.org/10.5281/zenodo.5562713>.
- Yang, M., T. Wang, and J. Shi (2021), Repeating infrasound from an earthquake doublet in Alaska, *Geophysical Research Letters*, 48(17), e2021GL094,632.
- 400